The International Journal of Advanced Manufacturing Technology (2023) 129:727–738
https://doi.org/10.1007/s00170-023-12324-x

ORIGINAL ARTICLE

Tailoring microbial response to stainless steel surfaces via electrolyte jet machining and electrodeposition

Adrian H. A. Lutey[1] · Luca Romoli[2] · Janggeon Lee[3] · Masanori Kunieda[3]

Received: 11 April 2023 / Accepted: 5 September 2023 / Published online: 21 September 2023

Abstract
Electrolyte jet machining (EJM) and electrodeposition present unexploited opportunities for the manufacturing of multiscale structured surfaces. The present work assesses the morphology and antibacterial properties of textured and multiscale stainless steel surfaces produced by EJM with a new 50 mm × 0.3 mm slit nozzle, as well as multiscale surfaces subject to electrodeposition with copper. Characterisation of the surface morphology obtained via EJM with various combinations of current density, machining time and groove spacing is performed to facilitate the selection of representative surfaces for bacterial retention tests. Higher current density with constant applied charge leads to lower surface roughness at constant scanning speed and greater groove depth and width under static conditions. Groove depth is proportional to machining time at constant current density, while a groove pitch of 1.05 mm is found to provide the optimum compromise between maximum groove depth and complete surface coverage. Microscale surface features are found to reduce *Escherichia coli* and *Pseudomonas aeruginosa* retention by up to 97% compared to untextured control surfaces, while larger grooves play a role in inhibiting bacterial attachment by inducing turbulence. The presence of copper agglomerates completely eliminates bacterial retention under the tested conditions. The developed process provides a flexible approach to tailoring surface properties for specific applications requiring antimicrobial properties.

Keywords Electrolyte jet machining (EJM) · Electrodeposition · Surface texture · Antimicrobial surfaces

1 Introduction

Textured surfaces with antimicrobial and antifouling properties have been the subject of intense scrutiny over recent years with the aim of overcoming contamination deriving from the build-up of bacteria, viruses, fungi and algae [1]. One of the most promising approaches has been the production of biomimetic structures mimicking naturally occurring surfaces such as the lotus leaf and cicada wing [2]. The former is characterised by the presence of hierarchical surface structures, facilitating self-cleaning behaviour via the rolling action of water droplets over the surface [3]. The latter comprises a series of nanoscale pillars that exhibit bactericidal properties via direct rupture of the cell wall [4]. Though a range of surface properties have been explored as drivers of antimicrobial behaviour, fine surface features similar in size or smaller than microbial cells (0.5–4 μm for bacteria) have been identified as playing a role in inhibiting retention during the initial phases of attachment by reducing the cell-substrate contact area [5]. Molecular dynamics modelling has shown that fine surface structures can create mechanical stresses within bacterial cell walls that, while not necessarily causing rupture, may be sufficient to induce changes in metabolism that inhibit proliferation [6]. This mechanism, shown schematically in Fig. 1, is more important than wettability for the functionality of textured antibacterial surfaces. Furthermore, wide and shallow periodic patterns may induce turbulent flow in liquid media that plays a role in limiting bacterial retention.

Manufacturing processes that have been employed for the production of textured antibacterial surfaces include sputter deposition [7], nanolithography [8] and short and ultrashort pulsed laser texturing [9, 10]. Sub-micrometric laser-induced

✉ Luca Romoli
luca.romoli@unipi.it

[1] Dipartimento Di Ingegneria E Architettura, Università Degli Studi Di Parma, 43124 Parma, Italy

[2] Dipartimento Di Ingegneria Civile E Industriale, Università Di Pisa, 56122 Pisa, Italy

[3] Department of Precision Engineering, School of Engineering, The University of Tokyo, Tokyo 113-8656, Japan

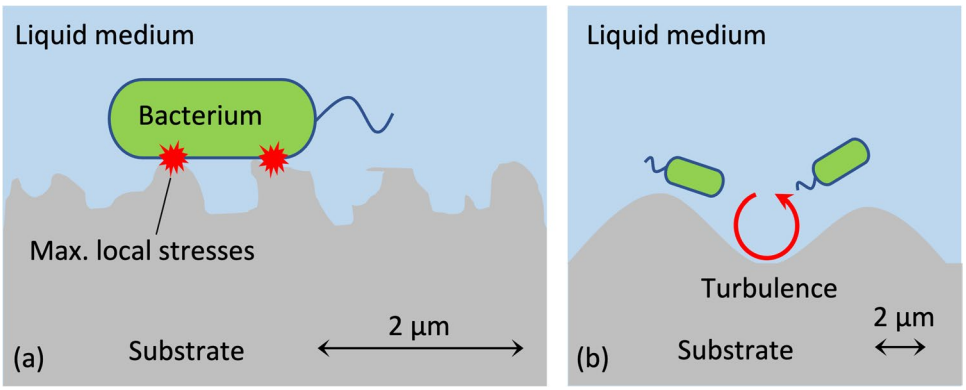

Fig. 1 Schematic representation of interaction between bacterial cells and a textured surfaces: **a** features smaller than the bacterium reduce contact area and intensify local stresses, inhibiting adhesion; **b** feature size and spacing larger than bacteria favour turbulence, avoiding nesting and formation of colonies at the bottom of valleys

periodic surface structures (LIPSS) produced with ultrashort laser pulses have been shown to reduce retention of *Escherichia coli* (*E. coli*) and *Pseudomonas aeruginosa* (*P. aeruginosa*) by as much as 99% [10, 11]. The formation of iron oxide via nanosecond pulsed laser texturing has also been shown to reduce *E. coli* retention by up to 98% [9]. Despite these outcomes, laser texturing exhibits important limitations relating to cost, thermal effects, uncontrolled changes in surface chemistry and difficulty in treating internal surfaces. Alternate manufacturing processes must therefore be pursued for the production of antimicrobial surfaces across a diverse range of applications.

In contrast to electrochemical machining (ECM), electrolyte jet machining (EJM) allows selective surface modification in a direct write manner and improves electrolyte supply to the reaction zone [12–14]. While ECM requires precise control over the distance between the tool and workpiece, EJM is performed at constant current density to achieve the same machined surface with little sensitivity to the distance between the electrodes. When performed at low current density, the surface can be textured by generating a fine structure via pitting corrosion. Recent developments in EJM have focused on increasing the resolution of achievable geometric features down to the microscale [15, 16]. While EJM is generally employed to produce well-defined features, attempting to maximise material removal rate and minimise error and roughness [17, 18], the ability to independently modify surface topography and chemistry in a single process has been shown to allow tailoring of surface wettability and biocompatibility [19, 20]. The surface morphology obtained via EJM depends on the current density and dwell time [21, 22], with the process allowing coarse, fine and multiscale features to be produced. When high current density is applied to the anode, dissolution phenomena are concentrated on surface protrusions, and the surface tends to become smooth, as the anodic dissolution rate is higher than the diffusion rate into the electrolyte. This results in the formation of a viscous liquid film consisting of dissolved metal ions near the surface. Since the diffusion layer is thicker in recesses than over protrusions, the dissolution rate of protrusions is faster than that of recesses. When the current density is low, the anodic dissolution rate is lower than the diffusion rate into the electrolyte, resulting in immediate diffusion of dissolved metal ions and uniform coverage of the metal surface by the diffusion layer. As a result, surface smoothing does not take place at low current density. These outcomes can be exploited to fabricate surfaces with various microstructures by EJM [21, 22]. A schematic of the relationship between the potential distribution and diffusion layer at low, intermediate and high current density is shown in Fig. 2.

Multiscale features produced via EJM have seen little attention to date despite their potential to play a role in the development of bio-inspired surfaces [23]. Turbulence can be generated when a fluid is made to flow over projections and depressions on a surface, an effect that can be exploited in conjunction with smaller surface structures to impede bacterial attachment. The pitch and

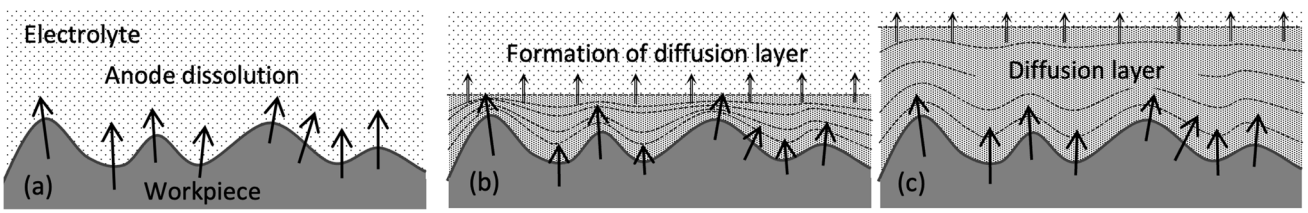

Fig. 2 Relationship between potential distribution and diffusion layer at **a** low, **b** intermediate and **c** high current density

depth of surface structures influence the degree of turbulence that is generated. Such structures can be produced via EJM with a slit nozzle by performing a series of stationary machining operations separated by a pre-defined distance perpendicular to the long edge of the nozzle. Slit nozzles also allow texturing to be performed with higher throughput than cylindrical nozzles [22, 23]; however, the geometry of EJM jets achieved with slit nozzles requires optimisation to ensure homogenous surface coverage and adequate throughput to compete with other processes such as laser texturing [24]. Finally, a similar process setup to EJM can be employed to perform electrodeposition, opening up a range of possibilities for coating textured multiscale metallic substrates with microbicidal elements such as silver and copper.

In light of these opportunities, the present work explores the potential of EJM and electrodeposition for the production of metallic antimicrobial surfaces, exploiting the antimicrobial properties of fine and multiscale surface structures produced via EJM by limiting the number of cell-substrate contact points and inducing turbulent flow in the liquid medium during the initial phases of attachment. Moreover, the biocidal properties of copper produced via electrodeposition are explored as an approach to reduce microbial retention. Further to the functional properties achieved with these electrochemical processes, a new slit nozzle is introduced for the treatment of 50-mm-wide samples in a single pass, representing a fundamental step towards upscaling and the production of larger functional surfaces.

2 Materials and methods

2.1 Substrates

Cold drawn SUS316 austenitic stainless steel substrates with initial roughness (S_a) of 0.19 ± 0.01 µm were employed for all experiments. Individual specimens were of dimensions 50 mm × 50 mm × 3 mm, providing sufficient area to perform microbial sampling from surfaces using contact swabs according to ISO 18593. Specimens were subject to various combinations of EJM and electrodeposition over the entire surface prior to bacterial retention tests.

2.2 EJM setup

The experimental setup employed for EJM, represented schematically in Fig. 3, consisted of a Matsusada Precision PKT 80–100 power supply, an Iwaki MDG-M4T6A100 Magnet Gear Pump electrolyte circulation system, a customised slit nozzle and Musasi Engineering SHOTMASTER 200DSS-4A CNC axes for movement in the x, y and z directions. The power supply was capable of providing voltage in the range 0–80 V and current in the range 0–100 A. The electrolyte was an aqueous solution of $NaNO_3$ (20 wt%). The nozzle consisted of two metal electrodes, a 0.3-mm spacer between the two and an insulating fixture to hold the assembly in place and confine the electrolyte. The width of the slit and thickness of the spacer determined the jet dimensions at the outlet, 50 mm × 0.3 mm. In contrast to previous studies employing slit nozzles of more limited width [25], the present setup employed a triangular pocket in the inlet fixture and a slot opening in one of the electrodes to

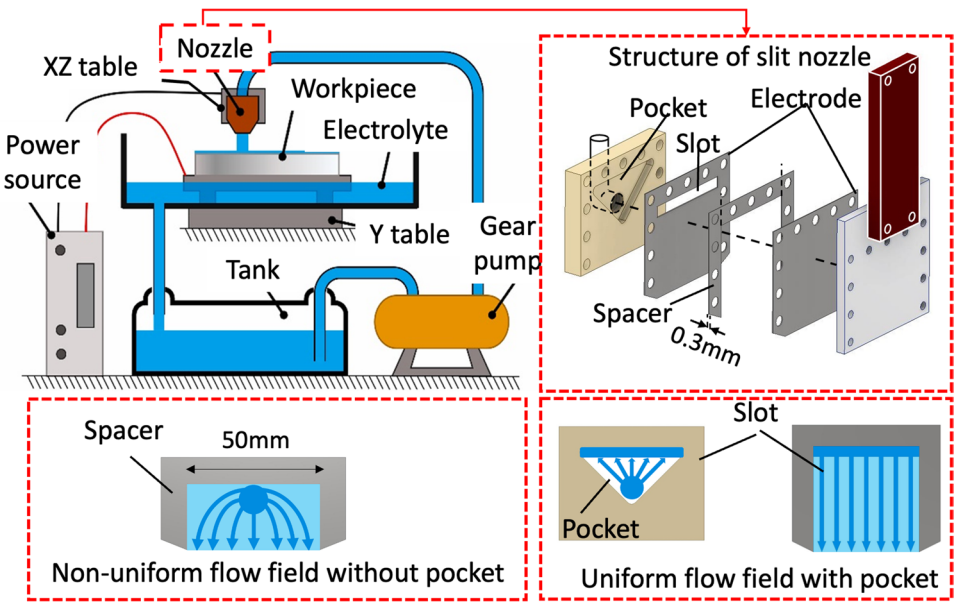

Fig. 3 Schematic of EJM setup, assembly of 50 mm × 0.3 mm slit nozzle, and influence of spacer and pocket on flow uniformity

provide uniform and stable flow across the entire width of the slit (see bottom right inset of Fig. 3). A thin wax layer was placed between the inlet-side insulating fixture and adjacent electrode to inhibit electrolyte leakage.

The potential and current density distribution achieved with a slit nozzle are fundamentally different to those achieved with a cylindrical nozzle. Figure 4 presents a comparison between the simulated potential difference and current density with cylindrical and slit nozzles [26, 27]. In both cases, the electric field strength immediately below the jet is high, with dissolution phenomena concentrated within this region. For the cylindrical nozzle, the electrolyte thickness immediately adjacent to the jet, *a/2*, is one quarter of the jet diameter, *2a*. For the slit nozzle, the electrolyte thickness in the same region, *a*, is half the slit width, *2a*. In addition, the current density decreases more quickly for the cylindrical nozzle than for the slit nozzle, reaching 1/10 of the peak value at *1.5a* from the centre of the cylindrical nozzle and *2a* from the centre of the slit nozzle. A slit nozzle therefore increases the area subject to low current density and can therefore be employed for surface texturing with higher throughput than a cylindrical nozzle [22].

2.3 Characterisation of EJM with 50 mm × 0.3 mm slit nozzle

EJM experiments were performed with a constant gap width of 1 mm. A homogeneous electrolyte distribution was achieved with a flow rate of at least 37 ml/s. Lower values led to a non-uniform jet distribution and dispersion in some cases, while higher values led to minor increases in jet width at distances far from the nozzle. A flow rate of 37 ml/s was considered to be the optimum compromise between obtaining a uniform jet and avoiding safety issues associated with rebound of the jet from the treated surface. The transparent nature of the jet was considered a positive indicator of electrolyte flow uniformity within the nozzle and machining region.

Four sets of experiments were performed to characterise the resulting surface morphology achieved with the 50 mm × 0.3 mm slit nozzle upon variation of the current density, machining time and groove spacing. With the aim of tailoring surface roughness, the effect of current density on the surface texture was firstly investigated at a constant scanning speed of 8 mm/s. In this case, the number of passes was chosen to be inversely proportion to the current density such that the applied charge per unit area was constant (Table 1). With the aim of tailoring multiscale surfaces, static machining experiments were then performed to investigate the effect of current density and machining time on the cross-sectional groove shape, depth and width. In a first set of experiments, the current density was varied, while the processing time was chosen to be inversely proportion to the current density such that the applied charge per unit area was constant (Table 2). In a second set of tests, a constant current density of 60 A/cm^2 was applied while varying the machining time independently (Table 3). Finally, the effect of groove pitch was investigated at a constant current density of 60 A/cm^2 and machining time of 8 s to determine the ideal spacing for production of homogeneous multiscale surfaces (Table 4).

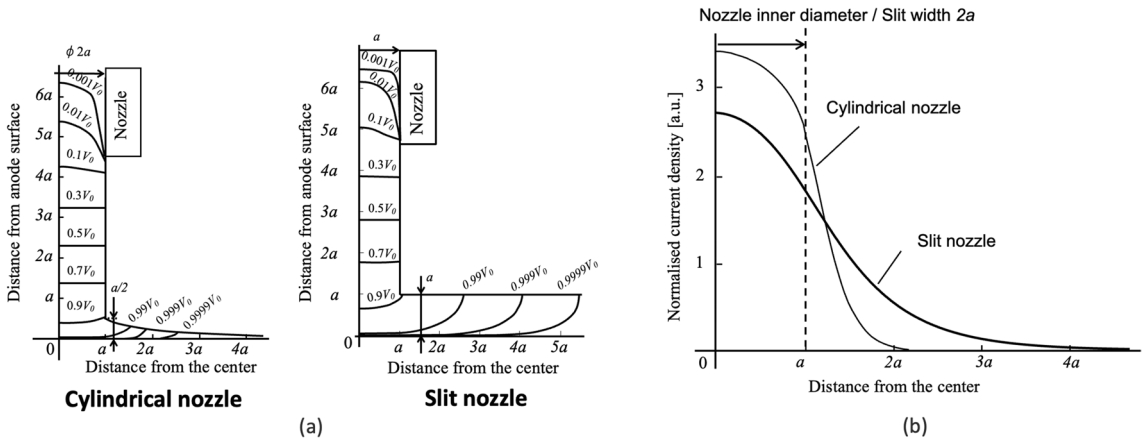

Fig. 4 **a** Potential distribution and **b** current density with cylindrical and slit nozzles [26, 27]

Table 1 EJM parameters employed for process characterisation at constant scanning speed

Current density (A/cm^2)	10	20	30	40	50	60
Scanning speed (mm/s)	8					
Number of passes	120	60	40	30	24	20

Table 2 EJM parameters employed for process characterisation under static conditions with constant applied charge

Current density (A/cm^2)	20	40	60	80	100
Machining time (s)	36	18	12	9	7.2

surface at a constant scanning speed of 8 mm/s. As with previous experiments, the number of scanning passes was chosen to maintain the same applied charge per unit area for all experiments, with 60 passes performed at 20 A/cm^2 and 20 passes performed at 60 A/cm^2. A second set of experiments was carried out with the aim of inducing local turbulence

Table 3 EJM parameters employed for process characterisation under static conditions at constant current density

Current density (A/cm^2)	60					
Machining time (s)	2	4	6	8	10	12

Table 4 EJM parameters employed for process characterisation under constant static conditions at constant current density and machining time

Current density (A/cm^2)	60					
Machining time (s)	8					
Groove spacing (mm)	0.95	1.00	1.05	1.10	1.15	1.20

Table 5 EJM and electrodeposition parameters employed for production of antimicrobial surfaces

Label	20 A/cm^2	60 A/cm^2	Multi.	Multi. + Cu
Current density, stationary (A/cm^2)	-	-	60	60
Machining time, stationary (s)	-	-	8	8
Groove spacing, stationary (mm)	-	-	1.05	1.05
Current density, scanning (A/cm^2)	20	60	20	20
Scanning speed, scanning (mm/s)	8	8	8	8
Number of passes, scanning	60	20	60	60
Solution, electrodeposition	-	-	-	$CuSO_4$
Current density, electrodeposition (A/cm^2)	-	-	-	0.15
Machining time, electrodeposition (s)	-	-	-	30

The surface morphology of all samples produced during this phase was acquired with a JEOL JSM-6010LV SEM. Linear profiles and roughness parameters were determined with a Mitutoyo SV-C3200S4.

2.4 EJM of antimicrobial surfaces

Based on the outcomes of these experiments, specific conditions were chosen to explore the effects of surface feature size and groove depth on the properties of antimicrobial surfaces. In order to decrease the contact area between the surface texture and bacterial cells as much as possible, a first set of experiments was performed to produce surface features less than 2 μm^2 in size. This theoretical value is the approximate cell-substrate contact area of rod-like (spherocylindrical) bacteria such as *E. coli* and *P. aeruginosa*, which have an average total length of 2 μm and diameter of 1 μm. Individual samples were treated with a current density of 20 A/cm^2 and 60 A/cm^2 while translating the nozzle across the in the liquid medium in close proximity to the substrate via multiscale surface structures. For this purpose, a series of stationary EJM operations was performed with a current density of 60 A/cm^2, machining time of 8 s and groove pitch of 1.05 mm, after which 60 translational passes were performed with a current density of 20 A/cm^2 and a scanning speed of 8 mm/s. A third set of experiments was performed with the aim of coating multiscale surfaces produced with the aforementioned procedure via electrodeposition of copper. Specimens were placed in an aqueous solution of $CuSO_4$ (20 wt%) together with pure copper anodes while passing a current density of 0.15 A/cm^2 between the two for 30 s. Copper was chosen due to its potential application in healthcare to reduce the risk of bacterial contamination [28]; however, the developed approach could also be applied to other biocidal elements. All process parameters employed for production of antimicrobial surfaces are presented in Table 5. A schematic of the entire manufacturing process for production of the antimicrobial surfaces is presented in Fig. 5.

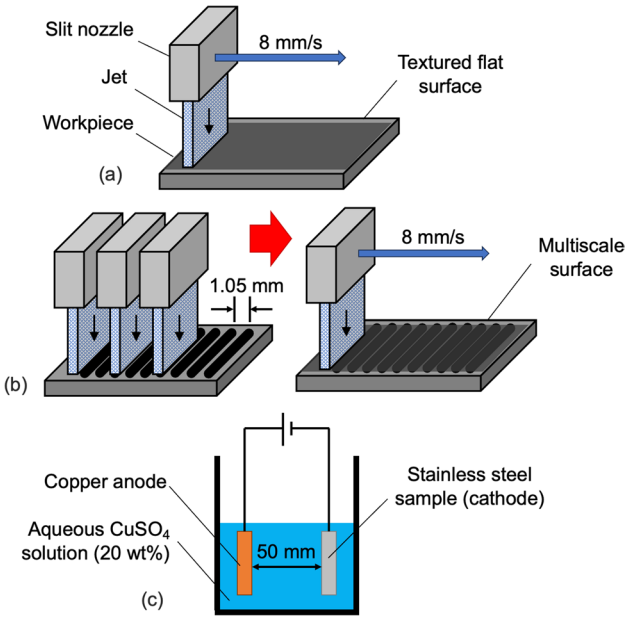

Fig. 5 Manufacturing process for the production of antimicrobial surfaces. **a** Textured flat surfaces subject to EJM at constant scanning speed (20 A/cm^2 and 60 A/cm^2). **b** Multiscale surfaces subject to stationary EJM operations followed by EJM at constant scanning speed. **c** Electrodeposition of copper on multiscale surfaces

Scanning electron microscopy (SEM) and energy-dispersive X-ray spectroscopy (EDX) were performed on treated and untreated samples with JEOL JSM-6010LV SEM and JSM-6510LV EDX systems to characterise surface morphology and chemistry, respectively. Surface topography was acquired with a Taylor Hobson CCI optical profiler equipped with 50× and 10× objectives. At highest magnification, the instrument was capable of achieving a resolution of 0.4 µm in the horizontal plane and < 1 nm in the vertical direction over an acquisition area of 356 µm × 356 µm. Topography analysis was performed at nine equally spaced positions on each sample at highest magnification to assess the uniformity of the applied treatments. For multiscale surfaces, a second order polynomial form filter was applied to remove surface curvature and allow only microscale topography to be assessed. Areal surface roughness parameters including the arithmetic mean height (S_a), skewness (S_{sk}), kurtosis (S_{ku}) and density of peaks (S_{pd}) were calculated in line with ISO 25178. Multiscale surfaces were also analysed at lower magnification over an area of 3 mm × 3 mm to acquire larger features for complete surface characterisation.

2.5 Bacterial retention

Bacterial retention tests were performed on treated and untreated samples following procedures set out in ISO 22196, ISO 27447 and ISO 18593 for measuring antibacterial performance and horizontal swabbing methods. Individual specimens were submerged in bacterial solutions and maintained in oscillation to assess bacterial attachment on textured and multiscale surfaces in dynamic conditions in line with the procedure described in [11]. *E. coli* and *P. aeruginosa* were chosen as bacterial strains due to their relevance in the food and healthcare industries. Both are rod-like gram-negative strains. Three identical samples were tested for each combination of bacteria type and surface, with the residual bacteria count normalised against results obtained on untreated SUS316 control samples tested under the same conditions. Bacterial colonies were incubated in Nutrient Agar (NA) at 37 °C to achieve an appropriate growth phase, after which the stock was diluted to N/500 before being transferred to sterile 200-ml containers. Cleaned and sterilised specimens were held horizontally within the bacterial solution for 2 h at 24 °C, with the tested surface facing upwards while the containers were agitated at 1.5 Hz with a stroke of 30 mm. Upon removal of the samples from the bacterial solution, surface swabs were taken over an area of 50 × 40 mm in both orthogonal directions prior to being diluted in solution and incubated in NA for 48 h at 37 °C. The number of colony forming units was then determined for each specimen with a colony counter.

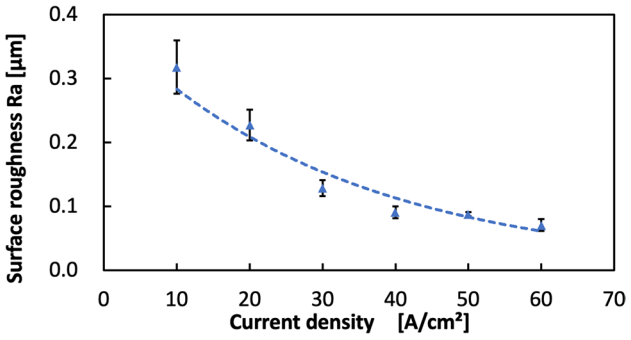

Fig. 6 Measured surface roughness as a function of current density for tests performed at a constant scanning speed of 8 mm/s

3 Results and discussion

3.1 Characterisation of EJM with 50 mm × 0.3 mm slit nozzle

The surface roughness obtained with tests performed at a constant scanning speed of 8 mm/s (Table 1) is displayed in Fig. 6. The surface roughness was found to decrease with increasing current density from approximately 0.3 µm at 10 A/cm^2 to approximately 0.1 µm at 60 A/cm^2, while the size of surface structures was also found to decrease with increasing current density. This outcome was due to

the anodic dissolution rate being lower than the electrolyte diffusion rate at low current density, resulting in uniform coverage of the surface by the diffusion layer (Fig. 2a). This led the formation of a complex, rough and porous surface structure at 10 A/cm^2 [21]. At higher current density, the anodic dissolution rate was higher than the electrolyte diffusion rate, resulting in more uniform coverage of the surface by the diffusion layer and preferential dissolution of protrusions, leading to smoothing of the surface and lower surface roughness at 60 A/cm^2 (Fig. 2c).

Based on these outcomes, higher current density was considered preferable for obtaining surface textures with fine surface features, appropriate for the production of antimicrobial surfaces. The cross-sectional groove shape, depth and width are shown in Fig. 7 for tests performed under static conditions (Table 2). Groove profiles exhibited typical rounded features with tapering due to changes in current density across the jet cross-section (Fig. 4b). Differences in processing depth and width were most pronounced between 20 and 40 A/cm^2, after which minor increases in groove depth were achieved at higher current density. Noting that the amount of charge per unit area was the same in all cases, much lower material removal at 20 A/cm^2 was due to the formation of a passive film on stainless steel in the sodium nitrate aqueous solution, which cannot be removed unless the current density is sufficient for the material to enter the hyperpassive region. Once this condition was overcome, the removal depth increased slowly with current density due to increases in current efficiency at higher current density [29]. Slight increases in groove width were also observed over the tested parameter range as more of the jet exceeded the activation threshold for the onset of machining.

For static tests performed at constant current density (Table 3), the processing depth was found to be proportional to the processing time (Fig. 8), in line with Faraday's law at constant current efficiency. Based on these outcomes, a processing time of 8 s was chosen to produce subsequent multiscale antimicrobial surfaces with a groove depth of approximately 50–60 µm. The effect of groove pitch on the resulting surface profile under these conditions (Table 4) is shown in Fig. 9. With a pitch of 1.00 mm, grooves were overlapping, leading to lower effective groove depth. With a pitch of 1.10 mm, a section of the original surface remained between grooves, leading to a discontinuous surface profile. A pitch of 1.05 mm was therefore selected as the optimum compromise between maximum groove depth and complete surface coverage.

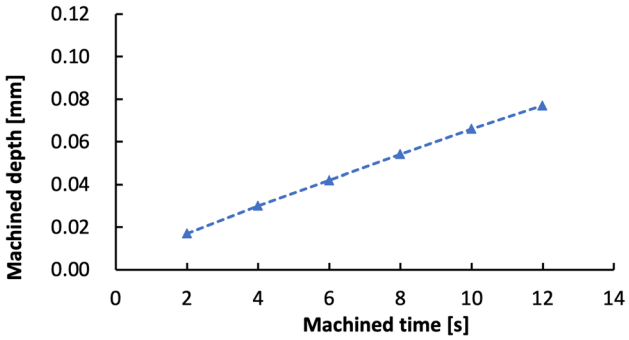

Fig. 8 Groove depth as a function of machining time for tests performed under static conditions with a constant current density of 60 A/cm^2

3.2 EJM of antimicrobial surfaces

SEM images of the antimicrobial surfaces produced via EJM and electrodeposition (Table 5) are presented in Fig. 10. Flat specimens treated with current densities of 20 A/cm^2 and

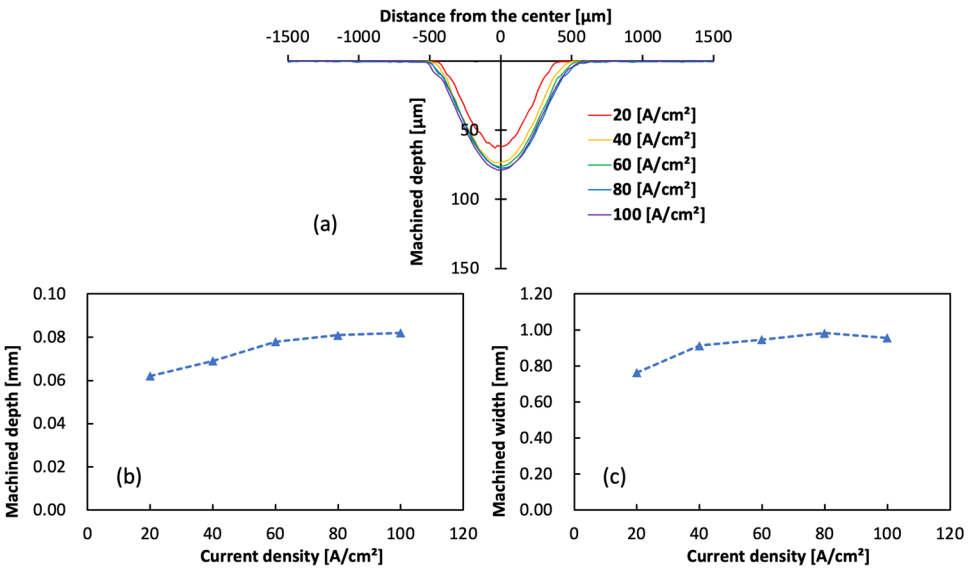

Fig. 7 Cross-sectional groove **a** shape, **b** depth and **c** width as a function of current density for tests performed under static conditions with constant applied charge

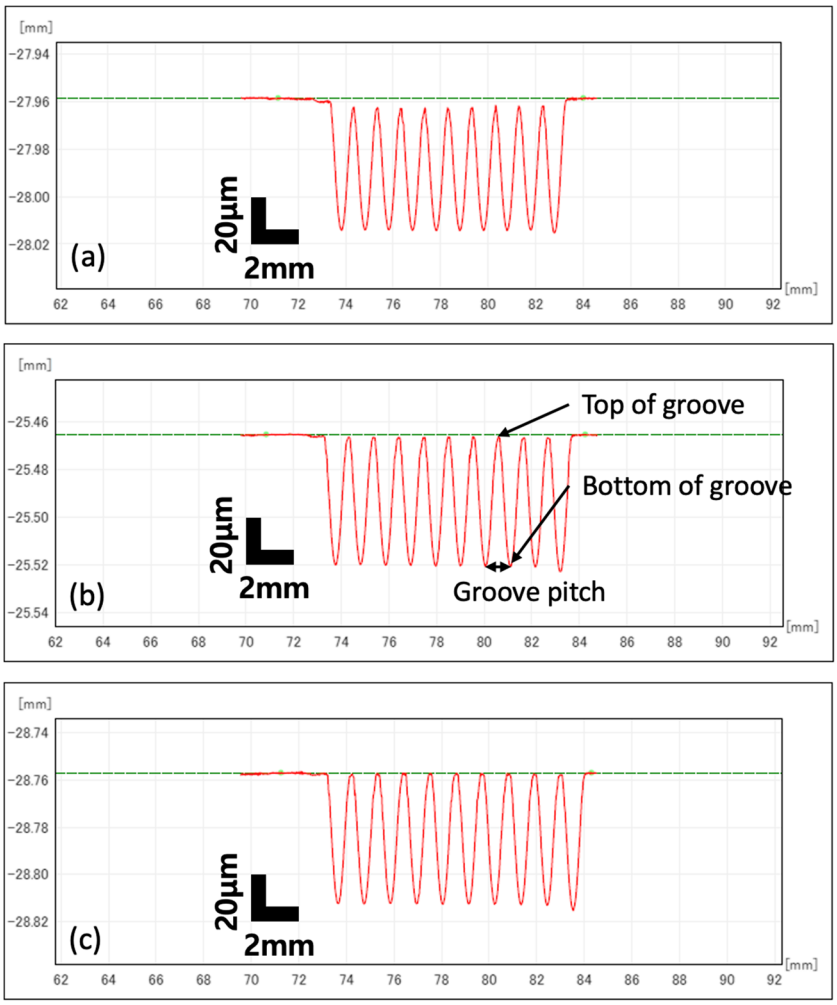

Fig. 9 Contour measurements of surfaces with groove pitches of **a** 1.00 mm, **b** 1.05 mm and **c** 1.10 mm and a current density of 60 A/cm^2 and machining time of 8 s. The original surfaces are indicated in green in each case

60 A/cm^2 with a constant scanning speed of 8 mm/s exhibited homogeneous arrays of craters ranging from < 1 µm to approximately 3 µm in diameter. Such morphology derived from pitting erosion during EJM [21]. Multiscale structures instead exhibited more complex morphology characterised by a series of macroscopic crests and valleys with a pitch of 1.05 mm, larger craters of diameter 10–30 µm on the top of each crest and homogeneous coverage of the entire surface with smaller craters similar to those observed on the flat samples. In this case, stationary EJM operations led not only to greater machining depth at the centre of the jet but also to the formation of large craters far from the electrolyte jet axis due to very low current density in these regions. Subsequent scanning passes led to the homogeneous formation of smaller craters, similar to those observed on flat textured samples, superimposed on the larger structures. Finally, electrodeposition with copper led to the formation of 1–5 µm agglomerates that partially covered the underlying texture. Though some of the finest surface features were masked during the deposition phase, the specimens were still characterised by hierarchical morphology comprising macroscopic crests, larger craters and finer surface features.

The atomic ratios of antimicrobial surfaces obtained with SEM–EDX are presented in Table 6. Flat textured and multiscale surfaces exhibited 4.3–4.9at.% increases in oxygen and 3.5–8.3at.% decreases in iron compared to reference samples as a result of reactions during the EJM process. Electrodeposition of copper instead led to approximately 50at.% copper, with large reductions in iron, chromium and nickel due to partial coverage of the original surface. This outcome confirmed that agglomerates formed during electrodeposition were in fact pure copper, thus incorporating an antimicrobial agent onto the textured surfaces.

Surface topographies acquired with the optical profiler are presented in Fig. 11 for multiscale antimicrobial surfaces. The presence of fine surface structures with vertical and horizontal dimensions in the order of 1–3 µm was observed on flat specimens and within the valleys of multiscale structures. The macroscopic peak-to-valley height of the latter was approximately 50 µm. Deposited agglomerates had a

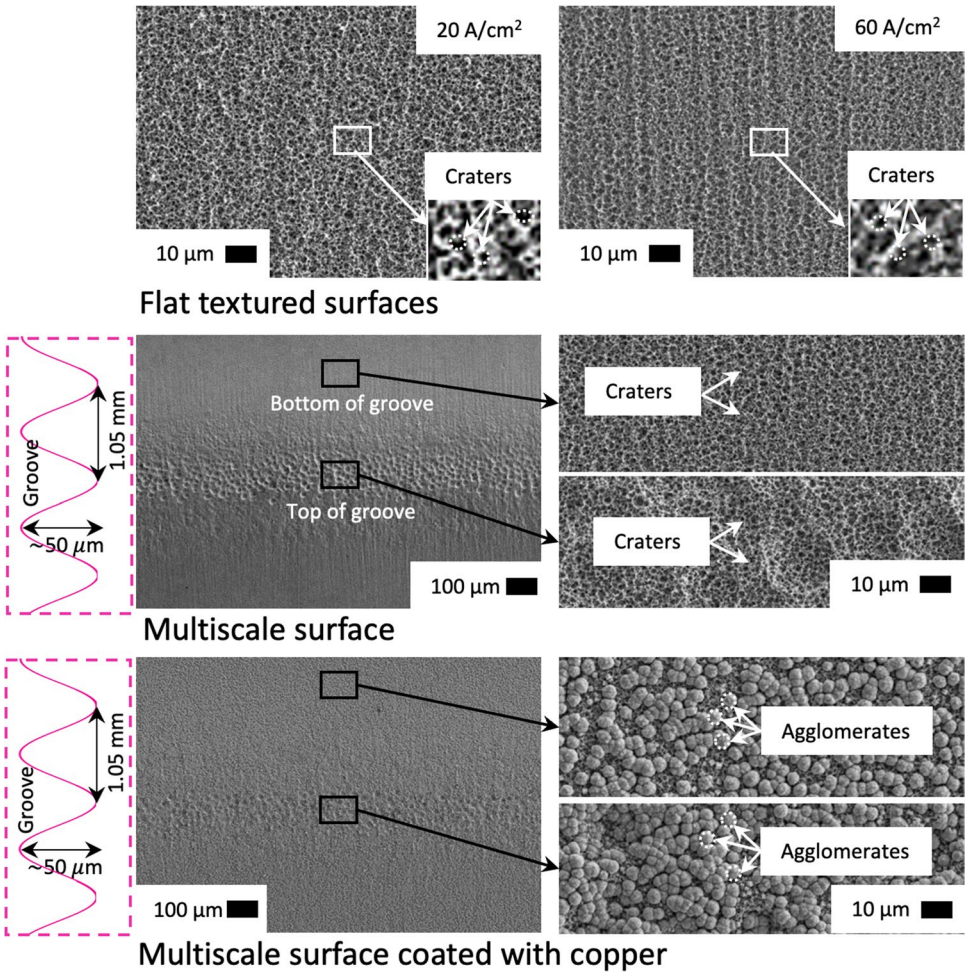

Fig. 10 SEM images of antimicrobial surfaces and schematics of multiscale surfaces

Table 6 Average SEM–EDX atomic ratios (at.%) of all antimicrobial surfaces

Sample	C	O	Cr	Fe	Ni	Cu	Other
Reference	16.2	1.5	15.6	57.3	7.8	-	1.6
20 A/cm^2	18.5	5.9	15.2	52.0	6.7	-	1.7
60 A/cm^2	22.0	6.4	14.8	49.0	6.4	-	1.5
Multi.	15.5	5.8	16.2	53.8	7.1	-	1.6
Multi. + Cu	19.6	3.1	5.8	19.5	1.9	49.8	0.3

clear impact on surface topography for specimens subject to electrodeposition with copper, leading to structures with vertical and horizontal extension in the order of 1–5 µm. A large proportion of the underlying topography was uniformly covered by copper agglomerates, with the presence of fine surface protrusions facilitating dense nucleation and adhesion of copper particles. Such adhesion to the surface texture is of importance for creating durable antimicrobial surfaces that may be subjected to turbulence of liquid media and other external forces.

Surface roughness parameters for antimicrobial surfaces are provided in Table 7. Flat textured and multiscale specimens exhibited marginally higher arithmetic mean height (S_a) than untextured reference samples, 0.23–0.26 µm compared to 0.19 µm, with a slight decrease with increasing current density. Electrodeposition with copper instead led to an approximately threefold increase in S_a to 0.75 µm due to important changes in surface topography. Skewness (S_{sk}) was in the range − 0.2 to 0.2 and kurtosis (S_{ku}) in the range 2–4 in all cases, corresponding to symmetric mesokurtic height distributions. The density of peaks (S_{pd}), calculated based on segmentation of the surface with the watershed algorithm, was in the range 0.58–0.63 µm^{-2} for flat textured and multiscale specimens, implying single features occupied on average 1.6–1.7 µm^2. This outcome is in line with the initial hypotheses for reducing retention of spherocylindrical

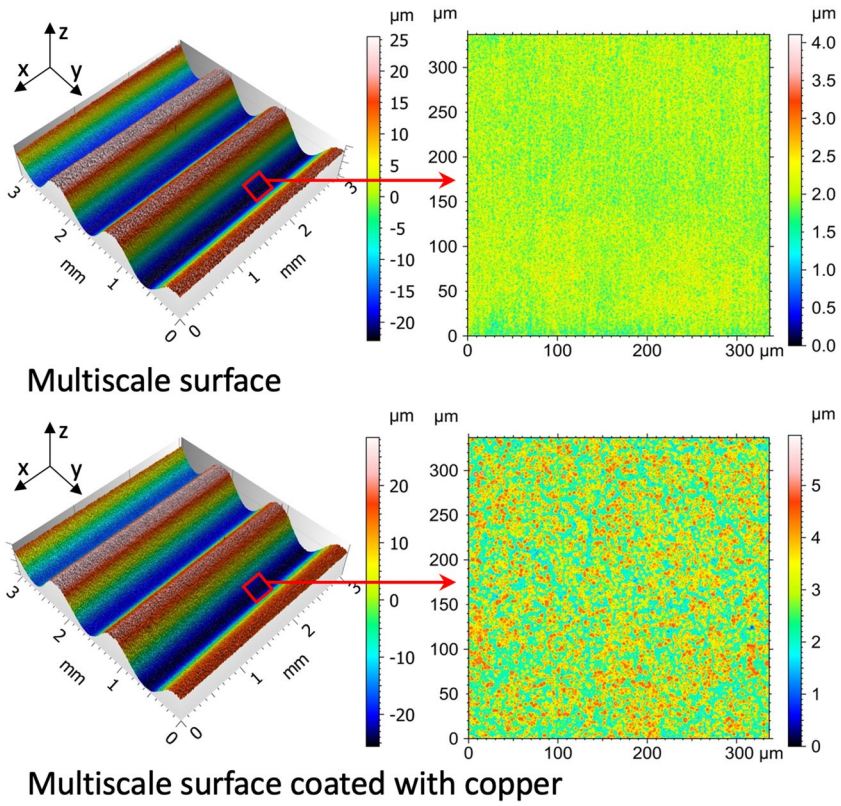

Fig. 11 Topographic maps of multiscale antimicrobial surfaces

Table 7 Average and standard deviation of areal surface roughness parameters for all tested specimens

Sample	S_a (µm)	S_{sk}	S_{ku}	S_{pd} (µm^{-2})
20 A/cm^2	0.26 ± 0.02	0.19 ± 0.06	3.95 ± 0.30	0.59 ± 0.02
60 A/cm^2	0.24 ± 0.02	−0.18 ± 0.04	3.25 ± 0.07	0.58 ± 0.01
Multi	0.23 ± 0.02	−0.10 ± 0.04	3.72 ± 0.13	0.63 ± 0.02
Multi. + Cu	0.75 ± 0.03	−0.13 ± 0.18	2.06 ± 0.27	0.46 ± 0.01

bacteria such as *E. coli* and *P. aeruginosa* on textured substrates, as the characteristic surface feature size must be similar or smaller than the cell-substrate contact area. The presence of larger features on multiscale surfaces was instead expected to have implications for avoiding bacterial nesting via the generation of turbulent flow conditions. Electrodeposition of copper led to a decrease in S_{pd} to 0.46 µm^{-2} due to the presence of larger surface features, implying single features occupied on average 2.2 µm^2. The standard deviation of all measured parameters was low, confirming that the slit nozzle provided homogeneous treatment over the entire 50 mm × 50 mm area of all specimens.

3.3 Bacterial retention

Average normalised residual bacteria counts for *E. coli* and *P. aeruginosa* are presented in Fig. 12 for all tested surfaces.

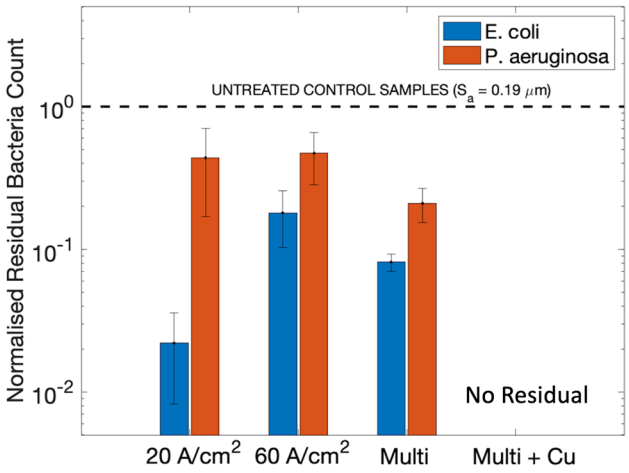

Fig. 12 Normalised bacterial retention on antimicrobial surfaces provided via EJM and electrodeposition

E. coli retention was reduced by more than 97% compared to untreated control samples for flat surfaces subject to a current density of 20 A/cm^2 and more than 90% for multiscale surfaces. As a consequence, *E. coli* was found to be more sensitive to the feature size generated by EJM than turbulent flow induced by larger-scale patterns on multiscale surfaces. Similar trends were observed for *P. aeruginosa* but with less pronounced reductions than for *E. coli*. In particular, *P.*

aeruginosa adhesion exhibited little dependence on the current density employed during EJM but moderate sensitivity to phenomena induced by multiscale features.

These outcomes confirmed the initial hypothesis that bacterial retention could be reduced by producing surface features with similar or smaller size than bacterial cells. The physical mechanism responsible for this reduction can be described by considering attachment point theory [5], whereby the available contact area between a textured substrate and an individual bacterium is greatly reduced during the initial phases of attachment as the surface feature size approaches the bacterial cell size. A smaller contact area leads to a reduction in adhesion strength, as individual cells have fewer attachment points than for larger surface features [30]. As a result, subsequent retention is inhibited or delayed, leading to surfaces that exhibit antibacterial behaviour. Both *E. coli* and *P. aeruginosa* are spherocylindrical bacteria with an average total length of 2 μm and diameter of 1 μm [31, 32], implying that the cell-substrate contact area is approximately 2 μm^2. All of the tested surfaces exhibited a density of peaks (S_{pd}, Table 7) in the range 0.46–0.63 μm^{-2}, implying single features occupied on average 1.6–2.2 μm^2, of similar magnitude to the cell-substrate contact area. This outcome implies that a reduction in adhesion strength was achieved due to the smaller contact area between the cell and substrate. The susceptibility of *P. aeruginosa* to multiscale features was instead linked to the influence of hydrodynamic phenomena on biofilm structure for this particular bacterium [33].

Bacterial retention was completely inhibited on multiscale surfaces subject to electrodeposition with copper, implying that the combination of surface topography and copper agglomerates was highly effective at inhibiting *E. coli* and *P. aeruginosa* attachment under the tested conditions. Copper is known to rapidly kill bacteria via several mechanisms, including the generation of reactive hydroxyl radicals that provoke harmful reactions to cellular molecules, as well as the depletion of sulfhydryls by copper ions and consequent generation of hydrogen peroxide [29]. The combination of reduced cell-substrate contact area and bactericidal properties of copper therefore led to robust antimicrobial performance of these surfaces under the tested conditions. Further investigation is now required to determine whether the tested surfaces exhibit antimicrobial behaviour over a wider spectrum of microorganisms, including different bacteria strains, viruses, fungi and algae.

4 Conclusion

The present study has demonstrated that EJM with a 50 mm × 0.3 mm slit nozzle and electrodeposition are versatile processes capable of producing antimicrobial surfaces exploiting various mechanisms to reduce contamination. After characterising the surface morphology obtained with various combinations of current density, machining time and groove spacing during EJM, representative surfaces were subject to bacterial retention tests to confirm the effectiveness of the proposed approach. Flat surfaces with fine surface features were found to greatly reduce *E. coli* attachment by limiting cell-substrate contact. Multiscale surfaces were found to be more effective against *P. aeruginosa* by also exploiting turbulent flow, while electrodeposition of copper was found to completely eliminate attachment of both bacteria. These outcomes provide proof of concept for development of multiscale bio-inspired surfaces via EJM and electrodeposition. The most suitable approach to manufacturing antimicrobial surfaces for a given application will depend on the specific microorganisms in question and tolerance to antimicrobial materials in sensitive environments such as food packaging or devices for water treatment. Further investigation is therefore required to test a wider range of microorganisms and alternate nozzle designs capable of treating surfaces with more complex geometry such as internal surfaces.

Author contribution AHAL: conceptualisation, methodology, validation, investigation, data curation, writing, original draft preparation, writing—reviewing and editing, and visualisation; LR: conceptualisation, validation, writing—original draft preparation, writing—reviewing and editing, visualisation, and supervision; JL: conceptualisation, data curation, validation, and writing—original draft preparation; and MK: writing, reviewing and editing, visualisation, and supervision. All authors read and approved the final manuscript.

Funding Open access funding provided by Università di Pisa within the CRUI-CARE Agreement. A part of this work was supported by "Advanced Research Infrastructure for Materials and Nanotechnology in Japan (ARIM)" of the Ministry of Education, Culture, Sports, Science and Technology (MEXT), Grant Number JPMXP1222UT0271.

Declarations

Competing interest The authors declare no competing interests.

References

1. Song B, Zhang E, Han X, Zhu H, Shi Y, Cao Z (2020) Engineering and application perspectives on designing an antimicrobial surface. ACS Appl Mater Inter 12:21330–21341. https://doi.org/10.1021/acsami.9b19992
2. Malshe AP, Bapat S, Rajurkar KP, Kaitjema H (2018) Bio-inspired textures for functional applications. CIRP Ann-Manuf Techn 67:627–650. https://doi.org/10.1016/j.cirp.2018.05.001
3. Long J, Fan P, Gong D, Jiang D, Zhang H, Li L, Zhong M (2015) Superhydrophobic surfaces fabricated by femtosecond laser with tunable water adhesion: from lotus leaf to rose petal. ACS Appl Mater Inter 7:9858–9865. https://doi.org/10.1021/acsami.5b01870
4. Kelleher SM, Habimana O, Lawler J, O'Reilly B, Daniels S, Casey E, Cowley A (2016) Cicada wing surface topography: an investigation into the bactericidal properties of nanostructural features. ACS Appl Mater Inter 8:14966–14974. https://doi.org/10.1021/acsami.5b08309
5. Whitehead KA, Verran J (2006) The effect of surface topography on the retention of microorganisms. Food Bioprod Process 84(C4):253–259. https://doi.org/10.1205/fbp06035
6. Lazzini G, Lutey AHA, Romoli L, Fuso F (2021) Molecular dynamics model for the antibactericity of textured surfaces. Colloid Surface B 199:111504. https://doi.org/10.1016/j.colsurfb.2020.111504
7. Sengstock C, Lopian M, Motemani Y, Borgmann A, Khare C, Buencosejo PJS, Schildhauer TA, Ludwig A, Köller M (2014) Structure-related antibacterial activity of a titanium nanostructured surface fabricated by glancing angle sputter deposition. Nanotechnology 25:195101. https://doi.org/10.1088/0957-4484/25/19/195101
8. Ito T, Okazaki S (2000) Pushing the limits of lithography. Nature 406:1027–1031. https://doi.org/10.1038/35023233
9. Romoli R, Lazzini G, Lutey AHA, Fuso F (2020) Influence of ns laser texturing of AISI 316L surfaces for reducing bacterial adhesion. CIRP Ann-Manuf Techn 69:529–532. https://doi.org/10.1016/j.cirp.2020.04.003
10. Fadeeva E, Truong VK, Stiesch M, Chichkov BN, Crawford RJ, Wang J, Ivanova EP (2011) Bacterial retention on superhydrophobic titanium surfaces fabricated by femtosecond laser ablation. Langmuir 27:3012–3019. https://doi.org/10.1021/la104607g
11. Lutey AHA, Gemini L, Romoli LG, Fuso F, Faucon M, Kling R (2018) Towards laser-textured antibacterial surfaces. Sci Rep 8:10112. https://doi.org/10.1038/s41598-018-28454-2
12. Kozak J (1989) Some aspects of electro jet drilling. In: Proceedings of Developments in Production Engineering Design & Control. Fourth Alexandria University PEDAC, Alexandria, pp 363–369
13. Kunieda M, Yoshida M, Yoshida H, Akamatsu Y (1993) Influence of micro indents formed by electro-chemical jet machining on rolling bearing fatigue life. ASME PED 64:693–699
14. Natsu W, Ikeda T, Kunieda M (2007) Generating complicated surface with electrolyte jet machining. Precis Eng 31:33–39. https://doi.org/10.1016/j.precisioneng.2006.02.004
15. Clare AT, Speidel A, Bisterov I, Jackson-Crisp A, Mitchell-Smith J (2018) Precision enhanced electrochemical jet processing. CIRP Ann-Manuf Techn 67:205–208. https://doi.org/10.1016/j.cirp.2018.04.086
16. Bisterov I, Abayzeed S, Speidel A, Magnini M, Zubayr M, Clare AT (2023) Adapting 'tool' size using flow focusing: a new technique for electrochemical jet machining. J Mater Process Tech 311:117807. https://doi.org/10.1016/j.jmatprotec.2022.117807
17. Kendall T, Bartolo P, Gillen D, Diver C (2019) A review of physical experimental research in jet electrochemical machining. Int J Adv Manuf Tech 105:651–667. https://doi.org/10.1007/s00170-019-04099-x
18. Kendall T, Diver C, Gillen D, Bartolo P (2022) New insights on manipulating the material removal characteristics of jet-electrochemical machining through nozzle design. Int J Adv Manuf Tech 118:1009–1026. https://doi.org/10.1007/s00170-021-07777-x
19. Yang X, Liu X, Lu Y, Zhou S, Gao M, Song J, Xu W (2016) Controlling the adhesion of superhydrophobic surfaces using electrolyte jet machining techniques. Sci Rep 6:23985. https://doi.org/10.1038/srep23985
20. Lu X, Leng Y (2005) Electrochemical micromachining of titanium surfaces for biomedical applications. J Mater Process Tech 169:173–178. https://doi.org/10.1016/j.jmatprotec.2005.04.040
21. Kawanaka T, Kato S, Kunieda M, Murry JW, Clare AT (2014) Selective surface texturing using electrolyte jet machining. Procedia CIRP 13:345–349. https://doi.org/10.1016/j.procir.2014.04.058
22. Kawanaka T, Kunieda M (2015) Mirror-like finishing by electrolyte jet machining. CIRP Ann-Manuf Techn 64:237–240. https://doi.org/10.1016/j.cirp.2015.04.029
23. Brinksmeier E, Karpuschewski B, Yan J, Schönemann L (2020) Manufacturing of multiscale structured surfaces. CIRP Ann-Manuf Techn 69:717–739. https://doi.org/10.1016/j.cirp.2020.06.001
24. Zhang J, Shen Z, Qu N (2022) Modelling and experimental investigation of flat surface achieved by large rectangular electrochemical jet milling. Int J Adv Manuf Tech 121:7933–7948. https://doi.org/10.1007/s00170-022-09897-4
25. Kunieda M, Mizugai K, Watanabe S, Shibuya N, Iwamoto N (2011) Electrochemical micromachining using flat electrolyte jet. CIRP Ann-Manuf Techn 60:251–254. https://doi.org/10.1016/j.cirp.2011.03.022
26. Yoneda K, Kunieda M (1995) Numerical analysis of cross sectional shape of micro-indents formed by the electrochemical jet machining (ECJM). J JSEME 29:1–8
27. Kawanaka T, Kunieda M (2013) C010 Micro ECM of curved patterns using shaped electrolyte jet. In: Proceedings of International Conference on Leading Edge Manufacturing in 21st Century: LEM21. LEM, pp 347–352. https://doi.org/10.1299/jsmelem.2013.7.347
28. Grass G, Rensing C, Solioz M (2010) Metallic copper as an antimicrobial surface. Appl Environ Microbiol 77:1541–1547. https://doi.org/10.1128/AEM.02766-10
29. Mitchell-Smith J, Speidel A, Clare AT (2018) Transitory electrochemical masking for precision jet processing techniques. J Manuf Process 31:273–285. https://doi.org/10.1016/j.jmapro.2017.11.028
30 Scardino AJ, Guenther J, de Nys R (2008) Attachment point theory revisited: the fouling response to a microtextured matrix. Biofouling 24:45–53. https://doi.org/10.1080/08927010701784391
31. Grossman N, Ron EZ, Woldringh CL (1982) Changes in cell dimensions during amino acid starvation of Escherichia coli. J Bacteriol 152:35–41. https://doi.org/10.1128/jb.152.1.35-41.1982
32. Baron S (ed) (1996) Medical microbiology. University of Texas Medical Branch at Galveston, Galveston
33. Purevdorj B, Costerton JW, Stoodley P (2002) Influence of hydrodynamics and cell signaling on the structure and behavior of Pseudomonas aeruginosa biofilms. Appl Environ Microb 68:4457–4464. https://doi.org/10.1128/AEM.68.9.4457-4464.2002